

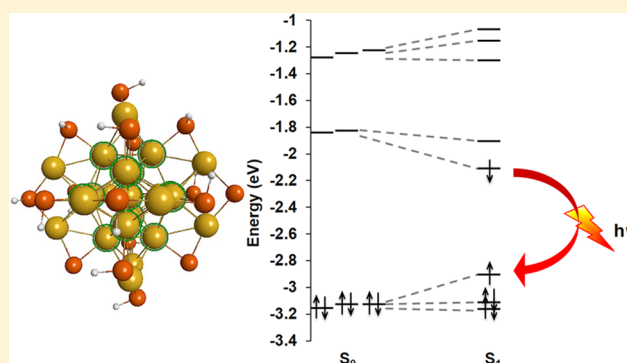
Theoretical Insights into the Origin of Photoluminescence of $\text{Au}_{25}(\text{SR})_{18}^-$ Nanoparticles

K. L. Dimuthu M. Weerawardene and Christine M. Aikens*

Department of Chemistry, Kansas State University, Manhattan, Kansas 66506, United States

S Supporting Information

ABSTRACT: Understanding fundamental behavior of luminescent nanomaterials upon photoexcitation is necessary to expand photocatalytic and biological imaging applications. Despite the significant amount of experimental work into the luminescence of $\text{Au}_{25}(\text{SR})_{18}^-$ clusters, the origin of photoluminescence in these clusters still remains unclear. In this study, the geometric and electronic structural changes of the $\text{Au}_{25}(\text{SR})_{18}^-$ ($\text{R} = \text{H}, \text{CH}_3, \text{CH}_2\text{CH}_3, \text{CH}_2\text{CH}_2\text{CH}_3$) nanoclusters upon photoexcitation are discussed using time-dependent density functional theory (TD-DFT) methods. Geometric relaxations in the optimized excited states of up to 0.33 Å impart remarkable effects on the energy levels of the frontier orbitals of $\text{Au}_{25}(\text{SR})_{18}^-$ nanoclusters. This gives rise to a Stokes shift of 0.49 eV for $\text{Au}_{25}(\text{SH})_{18}^-$ in agreement with experiments. Even larger Stokes shifts are predicted for longer ligands. Vibrational frequencies in the 75–80 cm^{-1} range are calculated for the nuclear motion involved in the excited-state nuclear relaxation; this value is in excellent agreement with vibrational beating observed in time-resolved spectroscopy experiments. Several excited states around 0.8, 1.15, and 1.25 eV are calculated for the $\text{Au}_{25}(\text{SH})_{18}^-$ nanocluster. Considering the typical underestimation of DFT excitation energies, these states are likely responsible for the emission observed experimentally in the 1.15–1.55 eV range. All excited states arise from core-based orbitals; charge-transfer states or other “semi-ring” or ligand-based states are not implicated.



INTRODUCTION

Gold nanoparticles (AuNPs) have received increasing research interest due to the tunability of their electronic and optical properties by changing size and shape, which enables a wide range of applications in chemical sensing,¹ biomedicine and imaging,² catalysis,^{3–5} photocatalysis,^{6–9} etc. To improve photocatalytic applications, a more complete understanding of the fundamental mechanisms involving photoexcitation and excited-state relaxation dynamics of these nanomaterials is required. During the past decade, luminescent AuNPs in the size range of 0.3–20 nm have been synthesized by tuning structural parameters like particle size, surface ligands, valence state, and grain size,¹⁰ and luminescence quantum yields of up to ~10% have been reported.^{11,12} Although the surface plasmon absorption of larger (5+ nm diameter) AuNPs as well as the discrete molecular-like absorption of gold nanoclusters with a core diameter of less than 2 nm are well studied and understood, the luminescence properties of AuNPs still remain unclear.

The observation of luminescence from bulk gold can be dated back to as early as 1969, when Mooradian observed photoluminescence of gold at 564 nm after excitation using a 488 nm laser.¹³ However, bulk gold has a very low quantum yield. About 30 years later, Kelley and co-workers¹⁴ identified blue emitting AuNPs with emission at 440 nm in systems with

diameters smaller than 5 nm. In 2000, luminescent gold nanorods emitting at 560 nm were reported.¹⁵ Shortly thereafter, Whetten and co-workers¹⁶ observed a novel near-infrared (1.1–1.6 μm) photoluminescence for AuNPs with core sizes of 1.1 and 1.7 nm with an estimated quantum yield of $(4.4 \pm 1.5) \times 10^{-5}$, which is more than 5 orders of magnitude greater than that of bulk gold. This photoluminescence was attributed to sp to sp-like (intraband) transitions. However, Huang and Murray¹⁷ reported visible wavelength fluorescence (700–800 nm) for four water-soluble monolayer-protected AuNPs with a core size smaller than 2 nm and hypothesized the luminescence mechanism to be associated with interband (d–sp) transitions. Furthermore, Murray and co-workers observed that five AuNPs with a wide range of gold cores (11–201 atoms) and protecting ligands emit over a similar range of energies from 700 nm (1.8 eV) to 1.3 μm (0.9 eV) when excited at 451 nm, and suggested that the core size-independence of the emission may be due to surface states related to the ligands rather than to core-based transitions.¹⁸ In comparison, Tsukuda and co-workers^{19,20} studied photoexcitation and emission of a group of glutathione protected gold nanoclusters having 18–39 gold atoms with photo-

Received: May 23, 2016

Published: August 15, 2016

luminescence quantum yields ranging from 1×10^{-3} to 7×10^{-4} . These clusters were found to emit around 1.6–1.8 eV with a maximum Stokes shift of 0.4 eV. They suggested that emission occurs from vibrationally relaxed states of the first electronically excited state.

Zheng et al.¹⁰ have summarized studies on different sized luminescent gold nanoparticles and the factors that influence luminescence properties and emission mechanisms. Therefore, only the luminescence of the thiolate protected 25-atom gold nanocluster will be discussed in the remainder of this Article. The crystallographic structure of the thiolate protected 25-atom gold nanocluster was solved in 2008.^{21,22} It consists of an approximately icosahedral Au_{13} core surrounded by six v-shaped $-\text{S}-\text{Au}-\text{S}-\text{Au}-\text{S}-$ staple motifs (sometimes called “semi-rings”) in an almost T_h symmetry (Figure 1).^{21–23} In

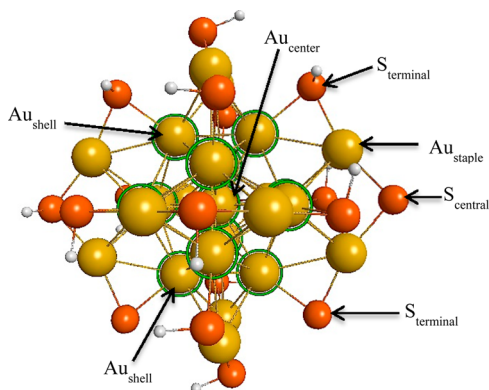


Figure 1. Structure of $\text{Au}_{25}(\text{SH})_{18}^-$. A shell of 12 gold atoms in an approximate icosahedron surrounds the central gold atom. The orange, yellow, black, and white color spheres represent sulfur, gold, carbon, and hydrogen atoms, respectively. This color code is consistent in all of the figures presented in this Article. The Au_{13} core gold atoms are marked with green circles.

2002, Link et al.^{24,25} reported luminescence extending over the visible to infrared region for the $\text{Au}_{25}(\text{SG})_{18}$ cluster (SG = glutathione). This nanocluster was originally mis-assigned as Au_{28} .^{26,27} They observed two different bands with maxima around 1.5 and 1.15 eV that indicated radiative recombination between the ground state and two excited states.²⁴ They proposed two possible models for the origin of the two luminescence bands: a “solid state” model in which the high and low energy bands correspond to interband and intraband (HOMO–LUMO) transitions, respectively, and a “molecular” model in which the two bands could be due to fluorescence and phosphorescence, respectively. The overall quantum yield for the cluster at ambient temperature was found to be $(3.5 \pm 1.0) \times 10^{-3}$. They also found that the luminescence decay dynamics are complex, which could be due to the presence of several closely spaced energy levels. Subsequently, Murray and co-workers²⁸ also reported two emission peaks at 1.38 and 1.2 eV for the $\text{Au}_{25}(\text{SR})_{18}$ ($\text{R} = \text{CH}_2\text{CH}_2\text{Ph}$) nanocluster, which was originally mis-assigned as Au_{38} . Because the HOMO–LUMO gap energy of 1.33 eV matched well with the 1.38 eV emission energy, they assigned this emission as relaxed luminescence across the HOMO–LUMO gap, while the 1.2 eV emission was thought to be sub-bandgap energy luminescence. They found that both emission peaks were strong when the nanocluster was excited at 680 nm, but that the 1.38 eV component was favored with higher energy (600 nm) excitation.

Pradeep and co-workers^{29,30} studied the photoluminescence and temperature-dependent solid-state emission of Au_{25} clusters. An emission peak at 700 nm was observed for $\text{Au}_{25}(\text{SG})_{18}$, whereas ligand exchange with a fluorescein-based dye red-shifted the peak by 25 nm.²⁹ This luminescence peak (~ 1.7 – 1.8 eV) is much higher in energy than the 1.38 or 1.5 eV emission bands observed previously. Furthermore, they observed that the ligand exchanged products of $\text{Au}_{25}(\text{SG})_{18}$ with acetyl- and formyl-glutathione give rise to similar emission spectra, whereas the 3-mercapto-2-butanol ligand blue-shifts the spectrum by 20 nm.³⁰ The observed emission was attributed to electronic transitions associated with the gold core, regardless of different ligands. In the temperature range of 80–300 K, the emission of $\text{Au}_{25}(\text{SG})_{18}$ occurred at the same position, which suggested that there are no major geometric changes in the system affecting its electronic structure.^{29,30} However, the intensity of the fluorescence was observed to decrease with decreasing temperature, suggesting that the nonradiative vibrational relaxation channel becomes prominent. Conversely, later work by Knappenberger and co-workers³¹ showed that the luminescence intensity of a neutral phenylethanethiolate-stabilized Au_{25} nanoparticle decreased as the temperature increased from 50 to 200 K.

Miller et al.³² studied the excited-state relaxation dynamics of $\text{Au}_{25}(\text{SCH}_2\text{CH}_2\text{Ph})_{18}^-$ with femtosecond laser spectroscopy. They excited the two lowest absorption peaks at 450 nm (assigned to an approximately 6-fold degenerate HOMO \rightarrow LUMO excitation) and 680 nm (approximately 9-fold degenerate HOMO \rightarrow LUMO+1 excitation) and watched the relaxation of the system until it reached the lowest-energy fluorescing state ($\lambda_{\text{em}} \approx 1000$ nm). They observed time constants greater than 4 ps measured at 725–800 nm detection wavelengths that they attributed to emission from “semi-ring” states (thought to be present below the HOMO–LUMO state arising from orbitals in the nanoparticle core) to the ground state. Furthermore, they detected an 80 cm^{-1} vibration localized to the Au_{13} core, which implies strong vibronic coupling of a delocalized Au–Au bond stretching vibration. Similar lifetimes (a short-lived ~ 1 ps component and a long-lived component) and phonon modes for the anionic $\text{Au}_{25}(\text{SR})_{18}$ cluster were later observed by Qian et al.,³³ but they suggested that the 80 cm^{-1} vibration is not an acoustic, spherically symmetric phonon mode as originally thought. In addition, they proposed that the electron dynamics they observed may be due to two slightly nondegenerate HOMO–LUMO transitions located in the core.

In 2006, Wang et al.³⁴ found that increasing the number of polar ligands on the nanocluster linearly increases the luminescence intensity of the near-infrared peak. Wu and Jin later studied the ligand and charge state dependence of fluorescence of $[\text{Au}_{25}(\text{SR})_{18}]^q$ nanoclusters.³⁵ Weak fluorescence around 750 nm was observed for $\text{Au}_{25}(\text{SR})_{18}^-$, and they found that the ligand’s ability to donate electron density to the metal core via the S–Au bond can enhance the fluorescence quantum yield. The intensity of the fluorescence signal was also observed to increase with the increasing electropositivity of the metal core (increasing q from -1 to $+2$). The observed fluorescence was attributed to a ligand to metal nanoparticle core charge transfer (LMNCT) mechanism. Recently, Wang et al.³⁶ reported similar results with Au_{25} nanoclusters protected by 2-(naphthalene-2-yl)ethanethiolate.

Ramakrishna, Goodson, and co-workers^{37–39} reported a low quantum yield visible photoluminescence (~ 500 nm) for

monolayer protected Au₂₅ nanoclusters in addition to near-infrared luminescence (around 710 nm for glutathione-protected nanoparticles³⁸ and around 830 nm³⁷ for hexanethiolate-protected nanoparticles) using ultrafast spectroscopy. They suggested that luminescence arises out of the Au₂₅ core states because the growth time constants are independent of the passivating ligand.³⁷ However, the ligand-dependent decay of luminescence was attributed to the relaxation of Au₂₅ core states to semi-ring states.³⁷

More recently, Knappenberger and co-workers³¹ studied temperature-dependent photoluminescence of neutral phenyl-ethanethiolate-stabilized Au₂₅ nanoparticles. Broad near-infrared photoluminescence was reported that consisted of several peaks at 1.72, 1.57, and 1.51 eV, implying multiple relaxation pathways. Increasing emission intensities were observed as the temperature was raised from 4.5 to 50 K. However, photoluminescence intensity decreased and red-shifted in energy at temperatures above 65 K. Two low-frequency vibrations associated with the ligand shell were identified: Au(I)–S stretching (180 cm⁻¹) and Au(0)–Au(I) stretching (105 cm⁻¹) that are responsible for nonradiative relaxation dynamics above 45 K. The amount of electronic–vibration coupling involved in each photoluminescence component was found to be state-specific and larger for the high-energy portions. (Table S1 summarizes the experimental photoluminescence results.)

Even though extensive experimental studies have been performed on synthesizing and characterizing luminescent monolayer protected Au₂₅ nanoclusters, their luminescence mechanism is still unclear. The luminescence has alternately been assigned to intraband and interband transitions, fluorescence and phosphorescence, surface or “semi-ring” states, or ligand–metal charge transfer states. Herein, we perform a theoretical investigation to determine the origin of the emission of Au₂₅(SR)₁₈⁻ (R = H, –CH₃, –CH₂CH₃, –CH₂CH₂CH₃) nanoclusters using density functional theory (DFT) and time-dependent density functional theory (TD-DFT) calculations.

COMPUTATIONAL METHODS

All geometry optimizations are performed using density functional theory (DFT) as implemented in the Amsterdam Density Functional (ADF) 2012.01 package.⁴⁰ The BP86 exchange-correlation functional^{41,42} and the double- ζ (DZ) basis set are used for all of the calculations. Generalized gradient approximation (GGA) functionals have been employed successfully in geometry relaxations and time-dependent DFT (TD-DFT) calculations of gold and silver nanoclusters previously.^{21,43–49} All structures are optimized in the gas phase. The energy and gradient convergence criteria are tightened to 1×10^{-4} and 1×10^{-3} to obtain well-converged geometries. Further tightening these values to 1×10^{-5} and 1×10^{-4} correspondingly gives energies lowered only by about a hundredth of an electronvolt with respect to the looser convergence criteria. Scalar relativistic effects are included by utilizing the zeroth-order regular approximation (ZORA). On the basis of the optimized ground-state geometries, the vertical excitations are calculated with the TD-DFT method using the same level of theory. The excited-state gradients are then calculated to optimize the excited-state geometry. Only singlet excited states (S_n) are considered here. Similar studies have been carried out to investigate luminescence properties of Au(I) complexes with thiolate and phosphine ligands.^{44,50} The experimental and theoretical results have shown a good agreement, even though calculated emission peak energies are around 0.3 eV lower than the experimental results. Herein, we calculate the optimized structure for excited states of Au₂₅(SR)₁₈⁻ (R = H, –CH₃, –CH₂CH₃, –CH₂CH₂CH₃) nanoclusters to

determine the origin of the emission in these systems. Stokes shifts are calculated by taking the energy differences between excitation and emission. For this, electronic ground and excited states are considered without accounting for vibrational contributions. All structures are visualized using the MacMolPlt⁵¹ visualization tool.

RESULTS AND DISCUSSION

1. Au₂₅(SH)₁₈⁻. The average bond lengths calculated at the BP86/DZ level of theory of the ground-state structure of Au₂₅(SH)₁₈⁻ in the gas phase are summarized in Table 1.

Table 1. Geometrical Parameters of the Ground-State and S_1 Excited-State Structures of Au₂₅(SH)₁₈⁻ at the BP86/DZ Level of Theory

| bond | average bond length (Å) | |
|---|-------------------------|-------------------------|
| | ground state (S_0) | excited state (S_1) |
| Au _{center} –Au _{shell} | 2.825 ± 0.003 | 2.846 ± 0.019 |
| Au _{shell} –Au _{shell} | 2.972 ± 0.073 | 2.995 ± 0.139 |
| Au _{shell} –S _{terminal} | 2.560 ± 0.005 | 2.566 ± 0.032 |
| Au _{staple} –S _{terminal} | 2.447 ± 0.006 | 2.452 ± 0.041 |
| Au _{staple} –S _{central} | 2.444 ± 0.002 | 2.457 ± 0.027 |

Within the Au₁₃ core, the average Au_{center}–Au_{shell} bond length is 2.825 ± 0.003 Å, whereas the Au_{shell}–Au_{shell} bond length is 2.972 ± 0.073 Å. These two bonds are 1.9% shorter and 3.2% longer, respectively, as compared to the Au–Au distance of 2.88 Å in bulk gold. The average Au_{shell}–S_{terminal} bond length is about 0.12 Å longer than the Au–S distances within the staple motifs.

The HOMO, HOMO–1, and HOMO–2 orbitals of Au₂₅(SR)₁₈⁻ (R = H, CH₃) are approximately triply degenerate and represent superatomic P orbitals delocalized over the Au₁₃ core.^{2f,23,52,53} (In many papers, these three orbitals are sometimes collectively referred to as the “HOMO”.) The ligand-field splitting from the six Au₂(SR)₃ units divides the unoccupied superatomic D orbitals into two sets: essentially doubly degenerate LUMO and LUMO+1 and essentially triply degenerate LUMO+2, LUMO+3, and LUMO+4.^{23,52,53} The “superatom electronic theory”^{23,54} has been successfully used to explain structure property relationships of various monolayer-protected AuNPs previously. Figure S1 demonstrates the Kohn–Sham orbitals of Au₂₅(SH)₁₈⁻ in the ground state, calculated at the BP86/DZ level of theory.

A time-dependent density functional theory (TD-DFT) calculation was performed on the relaxed ground-state geometry of Au₂₅(SH)₁₈⁻, and the first six singlet excited-state energies and the oscillator strengths are tabulated in Table 2. All of the states S_1 – S_6 vary within ~0.1 eV and correspond to HOMO, HOMO–1, or HOMO–2 to LUMO or LUMO+1 excitations. The oscillator strengths of the S_4 – S_6 states are 2 orders of magnitude higher as compared to the S_1 state that has

Table 2. Excited-State Energies and Oscillator Strengths for Au₂₅(SH)₁₈⁻ at the S_0 Geometry

| state | energy (eV) | oscillator strength (au) |
|-------|-------------|--------------------------|
| S_1 | 1.317 | 4.536×10^{-4} |
| S_2 | 1.320 | 1.277×10^{-3} |
| S_3 | 1.334 | 4.660×10^{-4} |
| S_4 | 1.403 | 2.374×10^{-2} |
| S_5 | 1.418 | 2.301×10^{-2} |
| S_6 | 1.433 | 2.337×10^{-2} |

an oscillator strength of 4.536×10^{-4} au. Moreover, the S_4 – S_6 states lie around 1.4 eV and represent the experimental absorption peak at 1.8 eV²¹ with an underestimation of approximately 0.4 eV. (It has been established^{43,55} that GGA functionals generally underestimate excitation energies.)

Herein, we calculate the optimized S_1 excited-state structure to determine the origin of the lowest energy emission of the $\text{Au}_{25}(\text{SH})_{18}^-$ nanocluster. Kasha's rule establishes that photon emission occurs in appreciable yield from the lowest excited state of a given multiplicity. Therefore, we initially consider the first excited state, S_1 . The fluorescence wavelength is the energy gap between the S_0 and S_1 states at the optimized S_1 state geometry. This energy gap calculated for the $\text{Au}_{25}(\text{SH})_{18}^-$ nanocluster is 0.83 eV, which corresponds to a fluorescence wavelength of 1495 nm. If one expects a similar 0.4 eV underestimation for the calculations relative to experiment, this would imply that the experimental emission from the S_1 state would occur around 1.2 eV, in good agreement with reported values of 1.15–1.2 eV.^{24,28} The oscillator strength for the emission is 2.462×10^{-3} au, which is 1 order of magnitude higher than that of the first excitation at the ground-state geometry. The emission energy is significantly smaller than the excitation energy of 1.32 eV, and thus the difference between the excitation energy and the emission energy is large. At the BP86/DZ level of theory, the Stokes shift calculated for the $\text{Au}_{25}(\text{SH})_{18}^-$ nanocluster is 0.49 eV. This is in good agreement with the Stokes shifts of around 0.4 eV found by Tsukuda et al.^{19,20}

Table 1 shows the geometrical parameters of the S_1 excited-state structure of $\text{Au}_{25}(\text{SH})_{18}^-$ in the gas phase. The average bond lengths of the ground-state structure increase by less than 0.03 Å upon formation of the optimized S_1 state geometry. However, several bonds lengthened considerably in the excited state. Table S2 shows the individual $\text{Au}_{\text{shell}}-\text{Au}_{\text{shell}}$ bond lengths that significantly differ between the ground- and excited-state geometries. The most prominent difference between S_0 and S_1 geometries is the elongation of 5–6 and 11–12 bonds by 0.25 Å in the S_1 optimized geometry. Sets of bonds 4–5, 10–11 and 5–7, 11–13 are also elongated by 0.10 Å as compared to the S_0 optimized geometry. While most of the $\text{Au}_{\text{shell}}-\text{S}_{\text{terminal}}$ bond lengths vary by less than 0.03 Å, Au_7-S and $\text{Au}_{13}-\text{S}$ bond lengths increase by about 0.06 Å. Consequently, the related $\text{Au}_{\text{staple}}-\text{S}_{\text{terminal}}$ and $\text{Au}_{\text{staple}}-\text{S}_{\text{central}}$ bond distances also increase by about 0.09 and 0.07 Å, respectively, in the optimized S_1 geometry. Calculated ground-state vibrational frequencies of the cluster demonstrated that the mode at 75.2 cm^{-1} corresponds to vibrations in Au_{13} core and specifically vibrations of the 5–6 and 11–12 bonds that have significant elongation in the S_1 state. These data suggest that the 75–80 cm^{-1} vibrations observed in various experimental studies^{32,33,37–39} of the excited-state dynamics of $\text{Au}_{25}(\text{SR})_{18}^-$ are likely due to the elongation of Au–Au bonds within the shell of the core during excited-state relaxation.

This geometry relaxation upon photoexcitation is related to a remarkable effect on the energy levels of the frontier orbitals of $\text{Au}_{25}(\text{SH})_{18}^-$ nanocluster. In fact, it is expected due to the Jahn–Teller effect that nuclear changes must occur when there is incomplete occupation of a set of degenerate (or in the case of $\text{Au}_{25}(\text{SR})_{18}^-$, nearly degenerate) orbitals, such as when there are five electrons in the P orbitals and one electron in the lowest set of D orbitals, as in the S_1 state of $\text{Au}_{25}(\text{SR})_{18}^-$. In fact, recently Ackerson and co-workers described the structural evolution of neutral and cationic counterparts of the

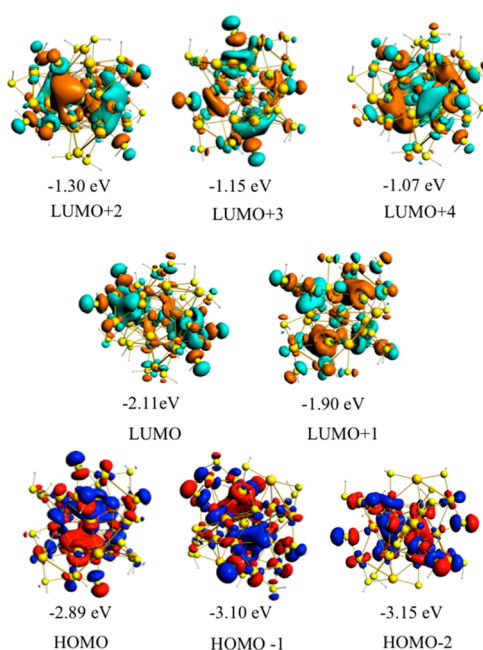


Figure 2. BP86/DZ Kohn–Sham orbitals and orbital energies for at the S_1 state of $\text{Au}_{25}(\text{SH})_{18}^-$. Isovalue = 0.02.

$\text{Au}_{25}(\text{SCH}_2\text{CH}_2\text{Ph})_{18}^-$ nanocluster using the Jahn–Teller effect.⁵⁶ Figure 2 demonstrates the Kohn–Sham orbitals for the S_1 state. Similar to Figure S1, these orbitals still retain their superatomic P and D character in the S_1 state geometry. The near triple-degeneracy of the highest occupied orbitals and the near double-degeneracy of the lowest unoccupied orbitals at the S_0 state geometry are disrupted for the optimized S_1 state. The HOMO is destabilized by 0.22 eV, whereas the LUMO is stabilized by 0.27 eV at the S_1 state as compared to that at the S_0 state geometry (Figure 3). As a result, the energy gap between the HOMO and LUMO decreases by 0.49 eV with the geometry relaxation at S_1 . Figure 3 demonstrates the splitting of frontier orbitals in the excited state with respect to the ground

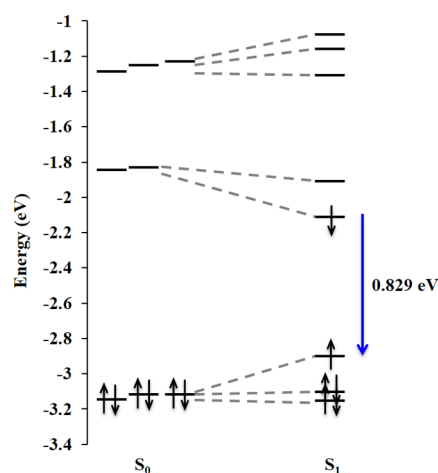


Figure 3. Comparison of energy levels of the frontier orbitals in S_0 and S_1 states. The S_1 state is shown in a cartoon representation with a single electron in one of the D orbitals. Dashed lines are drawn to show the splitting of triply degenerate HOMO/HOMO–1/HOMO–2, doubly degenerate LUMO/LUMO+1, and triply degenerate LUMO+2/LUMO+3/LUMO+4 orbitals of the ground state upon photoexcitation.

state. The splitting of superatomic P orbitals increases by 0.23 eV as compared to the S_0 state geometry, and the doubly degenerate D orbitals have a splitting of 0.20 eV in the S_1 state geometry. This type of splitting shows that the nanoparticle becomes less isotropic in the excited state.

Because the S_1 state is not the only state contributing to the luminescence of the $\text{Au}_{25}(\text{SR})_{18}^-$ nanocluster, we have also considered geometrical relaxation of other higher-lying states after photoexcitation. Although the calculation did not fully converge to our desired convergence criteria, excitation into the S_2 state results in geometrical changes similar to those of the S_1 state, with a similar Stokes shift. On the other hand, excitation into the S_3 state leads to much less dramatic changes in the bond lengths, with average $\text{Au}_{\text{shell}}-\text{Au}_{\text{shell}}$ bond lengths of 2.987 Å (Table 3) and a maximum increase of 0.069 Å in any of these

Table 3. Geometrical Parameters of the S_3 , S_5 , and S_7 Excited-State Structures of $\text{Au}_{25}(\text{SH})_{18}^-$ at the BP86/DZ Level of Theory

| bond | Average Bond Length (Å) | | |
|--|-------------------------|-----------------|-----------------|
| | S_3 structure | S_5 structure | S_7 structure |
| $\text{Au}_{\text{center}}-\text{Au}_{\text{shell}}$ | 2.838 ± 0.010 | 2.836 ± 0.009 | 2.833 ± 0.021 |
| $\text{Au}_{\text{shell}}-\text{Au}_{\text{shell}}$ | 2.987 ± 0.107 | 2.986 ± 0.105 | 2.981 ± 0.092 |
| $\text{Au}_{\text{shell}}-\text{S}_{\text{terminal}}$ | 2.564 ± 0.017 | 2.560 ± 0.012 | 2.582 ± 0.026 |
| $\text{Au}_{\text{staple}}-\text{S}_{\text{terminal}}$ | 2.447 ± 0.016 | 2.446 ± 0.014 | 2.454 ± 0.014 |
| $\text{Au}_{\text{staple}}-\text{S}_{\text{central}}$ | 2.453 ± 0.010 | 2.454 ± 0.008 | 2.457 ± 0.008 |

bonds. As a result, the orbitals maintain the near degeneracies observed in the ground state. In contrast to the S_1 optimized structure, the S_1-S_3 states are degenerate at 1.15 eV for the S_3 optimized structure. Optimization of the S_4 state appears to lead to results similar to those of S_3 . Like S_3 , excitation into the S_5 state also yields bond distances that are only slightly elongated as compared to the ground state; the average $\text{Au}_{\text{shell}}-\text{Au}_{\text{shell}}$ bond length is 2.986 Å with a maximum change of 0.064 Å in any of these bonds. At the optimized S_5 geometry, the S_4 and S_5 states are essentially degenerate at 1.247 eV. Excitation into the S_6 state also appears to lead to a very isotropic system. Although not fully converged to our desired convergence criteria, the S_1-S_3 states at the final S_6 geometry are essentially degenerate at 1.12–1.16 eV, and the S_4-S_6 states are essentially degenerate at about 1.25 eV.

Overall, these excited-state calculations suggest that several states could be responsible for the observed emission: a state calculated to lie around 0.8 eV (populated from photoexcitation into S_1 or S_2 , or transitions from higher states into these states), a state around 1.15 eV (populated from photoexcitation into S_3 or S_4 , or transitions from higher states into these states), or a state around 1.25 eV (populated from photoexcitation into S_5 or S_6 , or transitions from higher states into these states). Given the typical underestimation of GGA calculations, these states could yield the emission in the 1.15–1.55 eV (or similar) range observed experimentally.

Furthermore, we have also optimized the S_7 excited-state geometry. At the ground state, the S_7 state lies over 0.4 eV above the S_1-S_6 excited states. However, geometrical relaxation in the S_7 state leads to a dramatic decrease in the state energy to 1.46 eV. Given the typical underestimation of GGA calculations, the S_7 state likely lies too high in energy for the observed emission to arise from this state. However, optimization of the S_7 state leads to near-degeneracies with the S_6 and S_5 states (Table 4). This would facilitate

Table 4. Energies (eV) for the S_1-S_7 State Energies at Selected Optimized Excited-State Structures

| state | energy (eV) | | | |
|-------|-----------------|-----------------|-----------------|-----------------|
| | S_1 structure | S_3 structure | S_5 structure | S_7 structure |
| S_1 | 0.829 | 1.152 | 1.152 | 1.161 |
| S_2 | 1.059 | 1.153 | 1.159 | 1.223 |
| S_3 | 1.124 | 1.153 | 1.189 | 1.285 |
| S_4 | 1.148 | 1.247 | 1.247 | 1.367 |
| S_5 | 1.234 | 1.282 | 1.247 | 1.405 |
| S_6 | 1.354 | 1.286 | 1.324 | 1.456 |
| S_7 | N/A | N/A | 1.799 | 1.461 |

nonadiabatic excitation transfer to lower excited states, and could provide a mechanism by which higher excited states relax to the S_1-S_6 states. (Nonadiabatic electron relaxation will be addressed in upcoming work.)

2. $\text{Au}_{25}(\text{SR})_{18}^-$ ($R = \text{CH}_3, \text{CH}_2\text{CH}_3, \text{CH}_2\text{CH}_2\text{CH}_3$). To understand how the ligand affects the emission, we now discuss the geometric, electronic, and luminescence properties of the $\text{Au}_{25}(\text{SR})_{18}^-$ nanoclusters, where the alkyl ligand R increases in length from methyl to propyl. Table 5 summarizes the average bond lengths of the ground-state structures of these clusters in the gas phase. The average $\text{Au}_{\text{shell}}-\text{S}_{\text{terminal}}$ bond lengths are shortened by about 1% in the ground-state structures with alkyl ligands as compared to $\text{Au}_{25}(\text{SH})_{18}^-$. However, Au–Au bond lengths do not vary noticeably with the changing ligand.

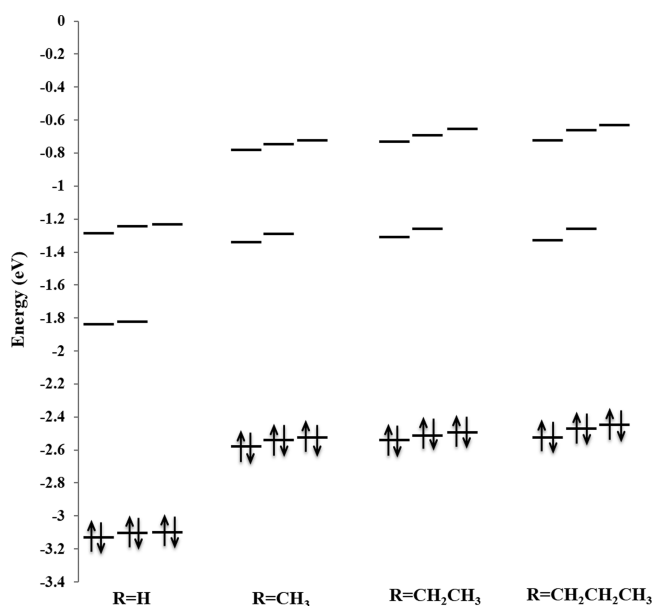
The ground-state electronic structure of $\text{Au}_{25}(\text{SCH}_3)_{18}^-$ is significantly affected by changing the ligand from H to methyl. However, further increasing the carbon chain length from methyl to propyl has only slight effects on the ground-state electronic structure of these nanoclusters. Figure 4 and Table S3 compare ground-state energy levels of the frontier orbitals and HOMO–LUMO gaps of $\text{Au}_{25}(\text{SR})_{18}^-$ ($R = \text{H}, \text{CH}_3, \text{CH}_2\text{CH}_3, \text{CH}_2\text{CH}_2\text{CH}_3$) nanoclusters. The essentially triply degenerate HOMO/HOMO–1/HOMO–2 orbitals are destabilized by 0.6 eV, whereas the doubly degenerate LUMO/LUMO+1 and triply degenerate LUMO+2/LUMO+3/LUMO+4 orbitals are destabilized by 0.5 eV upon changing the ligand from H to methyl. Nevertheless, the splitting of the P and D orbital sets increased only by 0.03, 0.05, and 0.01 eV due to the ligand variation from H to methyl. When the ligand is changed from methyl to propyl, the frontier orbitals are generally destabilized by a few hundredths of an electronvolt.

We performed TD-DFT calculations based on the relaxed ground-state geometries of methyl-, ethyl-, and propyl-thiolate protected Au_{25} nanoclusters. The first six singlet excited-state energies and the oscillator strengths of $\text{Au}_{25}(\text{SR})_{18}^-$ nanoclusters are tabulated in Table S4. The S_1 state energy of $\text{Au}_{25}(\text{SR})_{18}^-$ ($R = \text{CH}_3, \text{CH}_2\text{CH}_3, \text{CH}_2\text{CH}_2\text{CH}_3$) is increased correspondingly by 0.08, 0.06, and 0.13 eV from that of $\text{Au}_{25}(\text{SH})_{18}^-$. The oscillator strength of the first excited state is increased by 1 order of magnitude, whereas that of the S_4, S_5 , and S_6 states are not changed significantly for these three clusters as compared to $\text{Au}_{25}(\text{SH})_{18}^-$. The prominent peak that arises due to S_4-S_6 states in the optical absorption spectra of $\text{Au}_{25}(\text{SR})_{18}^-$ is red-shifted by ~0.1 eV upon substituting the H-ligand by alkyl ligands. However, the S_1 state energy is increased by 0.02 eV from methyl to ethyl thiolate ligated cluster, whereas it is reduced by 0.07 eV from ethyl to propyl.

Next, the optimized excited-state structures of $\text{Au}_{25}(\text{SR})_{18}^-$ ($R = \text{CH}_3, \text{CH}_2\text{CH}_3, \text{CH}_2\text{CH}_2\text{CH}_3$) nanoclusters are calculated to determine the origin of their emission. In this section, we

Table 5. Geometrical Parameters of the Ground-State and Excited-State Structures of $\text{Au}_{25}(\text{SR})_{18}^-$ at the BP86/DZ Level of Theory

| bond | average bond length (Å) | | | | | |
|--|---------------------------------------|-------------------|--|-------------------|---|-------------------|
| | $\text{Au}_{25}(\text{SCH}_3)_{18}^-$ | | $\text{Au}_{25}(\text{SCH}_2\text{CH}_3)_{18}^-$ | | $\text{Au}_{25}(\text{SCH}_2\text{CH}_2\text{CH}_3)_{18}^-$ | |
| | S_0 | S_1 | S_0 | S_1 | S_0 | S_1 |
| $\text{Au}_{\text{center}}-\text{Au}_{\text{shell}}$ | 2.831 ± 0.004 | 2.858 ± 0.031 | 2.828 ± 0.006 | 2.852 ± 0.027 | 2.830 ± 0.009 | 2.859 ± 0.033 |
| $\text{Au}_{\text{shell}}-\text{Au}_{\text{shell}}$ | 2.978 ± 0.089 | 3.009 ± 0.177 | 2.976 ± 0.088 | 3.001 ± 0.157 | 2.977 ± 0.095 | 3.012 ± 0.188 |
| $\text{Au}_{\text{shell}}-\text{S}_{\text{terminal}}$ | 2.539 ± 0.003 | 2.546 ± 0.028 | 2.534 ± 0.005 | 2.543 ± 0.030 | 2.539 ± 0.005 | 2.559 ± 0.041 |
| $\text{Au}_{\text{staple}}-\text{S}_{\text{terminal}}$ | 2.431 ± 0.010 | 2.434 ± 0.033 | 2.431 ± 0.011 | 2.438 ± 0.036 | 2.431 ± 0.011 | 2.442 ± 0.037 |
| $\text{Au}_{\text{staple}}-\text{S}_{\text{central}}$ | 2.430 ± 0.003 | 2.443 ± 0.021 | 2.430 ± 0.003 | 2.444 ± 0.022 | 2.430 ± 0.002 | 2.448 ± 0.023 |

**Figure 4.** Comparison of ground-state orbital energy levels of $\text{Au}_{25}(\text{SR})_{18}^-$ nanoclusters.

consider the first excited state, S_1 , only. The fluorescence wavelengths and the calculated Stokes shifts for these three clusters are compared to $\text{Au}_{25}(\text{SH})_{18}^-$ in Table 6. It should be

Table 6. Comparison of Emission Energies (Fluorescence Wavelengths) and Stokes Shifts

| nanocluster | emission | | Stokes shift | |
|---|-------------|-----------------|--------------|-----------------|
| | energy (eV) | wavelength (nm) | energy (eV) | wavelength (nm) |
| $\text{Au}_{25}(\text{SH})_{18}^-$ | 0.829 | 1495 | 0.488 | 553 |
| $\text{Au}_{25}(\text{SCH}_3)_{18}^-$ | 0.655 | 1892 | 0.579 | 887 |
| $\text{Au}_{25}(\text{SCH}_2\text{CH}_3)_{18}^-$ | 0.692 | 1791 | 0.563 | 803 |
| $\text{Au}_{25}(\text{SCH}_2\text{CH}_2\text{CH}_3)_{18}^-$ | 0.512 | 2424 | 0.676 | 1379 |

noted that because of the inverse relationship between energy and wavelength, small changes in energy in the near-IR region result in large changes in the wavelength. The emission energy decreases by 0.17 eV upon changing the SH ligand to SCH_3 . However, when the alkyl ligand is changed from methyl to ethyl, the emission energy is increased by 0.037 eV, and it is reduced by 0.18 eV when the ligand is changed from ethyl to propyl similar to the trend observed for the S_1 state energy. Furthermore, Stokes shifts have the same trend with the increasing length of the alkyl ligand as shown in Table 6. The large Stokes shifts can be attributed to the notable modifications in the geometric and electronic structures of

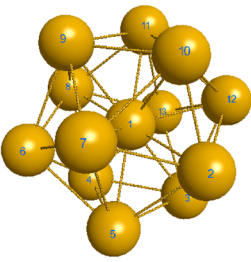
the optimized S_1 states of these clusters as compared to their S_0 states. This Stokes shift trend suggests that the largest geometrical changes occur in the excited state of the propylthiolate-protected Au_{25} cluster, followed by methylthiolate- and then ethylthiolate-protected clusters.

Table 5 summarizes the excited-state geometrical parameters of $\text{Au}_{25}(\text{SR})_{18}^-$ ($R = \text{H}, \text{CH}_3, \text{CH}_2\text{CH}_3, \text{CH}_2\text{CH}_2\text{CH}_3$) nanoclusters in the gas phase. Analogous to $\text{Au}_{25}(\text{SH})_{18}^-$, the average bond lengths of the ground-state structures of $\text{Au}_{25}(\text{SR})_{18}^-$ change by less than 0.04 Å upon formation of the optimized S_1 state geometries. However, the increased standard deviations of $\text{Au}_{\text{shell}}-\text{Au}_{\text{shell}}$ bond lengths show that several bonds vary considerably in the excited state. Table 7 lists the individual $\text{Au}_{\text{shell}}-\text{Au}_{\text{shell}}$ bond lengths that significantly differ between the ground- and excited-state geometries.

As listed in Table 7, the largest bond increases (bonds 2–3 and 8–9) in $\text{Au}_{25}(\text{SCH}_3)_{18}^-$, $\text{Au}_{25}(\text{SCH}_2\text{CH}_3)_{18}^-$, and $\text{Au}_{25}(\text{SCH}_2\text{CH}_2\text{CH}_3)_{18}^-$ are 0.28, 0.23, and 0.33 Å, respectively. This correlates with the smallest Stokes shift found for ethyl and the greatest Stokes shift calculated for propyl. Bonds 4–3, 9–10, 5–6, 11–12, 8–13, and 2–7 are shortened in the excited states of $\text{Au}_{25}(\text{SR})_{18}^-$ as compared to the related ground-state geometries. The essentially icosahedral Au_{13} core of the $\text{Au}_{25}(\text{SR})_{18}^-$ clusters diverges even more from a true icosahedron due to these bond length changes in the excited state. As shown for the $\text{Au}_{25}(\text{SH})_{18}^-$ cluster in the previous section, these geometrical changes can affect the energy levels of the frontier orbitals of $\text{Au}_{25}(\text{SR})_{18}^-$ clusters significantly. Figure 5 and Table S5 demonstrate the splitting of frontier orbitals in the excited states of $\text{Au}_{25}(\text{SR})_{18}^-$ clusters with respect to their ground states.

Upon excitation, the HOMO orbitals of $\text{Au}_{25}(\text{SR})_{18}^-$ ($R = \text{H}, \text{CH}_3, \text{CH}_2\text{CH}_3, \text{CH}_2\text{CH}_2\text{CH}_3$) clusters are destabilized by 0.33, 0.28, and 0.34 eV, whereas the LUMO orbitals are stabilized by 0.25, 0.27, and 0.34 eV, respectively. This gives rise to a large HOMO–LUMO gap reduction of 0.67 eV for the $\text{Au}_{25}(\text{SCH}_2\text{CH}_2\text{CH}_3)_{18}^-$ cluster. Moreover, HOMO–LUMO energy gaps are reduced by 0.58 and 0.55 eV in the relaxed excited-state geometries of methyl- and ethyl-thiolate protected Au_{25} clusters. However, LUMO+2, LUMO+3, and LUMO+4 orbitals of all three clusters do not vary significantly. The approximate degeneracy of the highest occupied orbitals in the S_0 state is again lost in the S_1 state. The highest splitting of these orbitals is 0.5 eV in the S_1 state of $\text{Au}_{25}(\text{SCH}_2\text{CH}_2\text{CH}_3)_{18}^-$ cluster, whereas a splitting of 0.4 eV can be observed for methyl and ethyl-thiolate protected clusters. Similarly, the approximate double-degeneracy of the lowest unoccupied orbitals with a maximum splitting of 0.07 eV for these three clusters in the S_0 state is increased by ~ 0.2 eV in their S_1 states.

Table 7. Comparison of $\text{Au}_{\text{shell}}-\text{Au}_{\text{shell}}$ Bond Lengths in Relaxed Geometries of the Ground State (S_0) and the First Excited State (S_1) of the $\text{Au}_{25}(\text{SR})_{18}^-$ Nanoclusters

| Au_{13} - core Structure | Bond | Bond Length (Å) | | | | | |
|---|---------|---------------------------------------|-------|--|-------|---|-------|
| | | $\text{Au}_{25}(\text{SCH}_3)_{18}^-$ | | $\text{Au}_{25}(\text{SCH}_2\text{CH}_3)_{18}^-$ | | $\text{Au}_{25}(\text{SCH}_2\text{CH}_2\text{CH}_3)_{18}^-$ | |
| | | S_0 | S_1 | S_0 | S_1 | S_0 | S_1 |
|  | 4 - 3 | 3.002 | 2.906 | 3.018 | 2.932 | 3.017 | 2.898 |
| | 9 - 10 | 3.002 | 2.904 | 3.017 | 2.932 | 3.017 | 2.897 |
| | 4 - 13 | 3.077 | 3.190 | 3.065 | 3.152 | 3.089 | 3.299 |
| | 7 - 10 | 3.076 | 3.195 | 3.062 | 3.151 | 3.088 | 3.299 |
| | 5 - 6 | 3.075 | 2.954 | 3.084 | 2.966 | 3.100 | 3.041 |
| | 11 - 12 | 3.079 | 2.956 | 3.080 | 2.965 | 3.100 | 3.041 |
| | 6 - 8 | 3.028 | 3.257 | 3.014 | 3.232 | 3.042 | 3.206 |
| | 2 - 12 | 3.021 | 3.248 | 3.014 | 3.235 | 3.042 | 3.206 |
| | 8 - 13 | 3.012 | 2.895 | 3.021 | 2.905 | 2.991 | 2.899 |
| | 2 - 7 | 3.013 | 2.897 | 3.022 | 2.904 | 2.991 | 2.899 |
| | 2 - 3 | 3.088 | 3.360 | 3.064 | 3.290 | 3.110 | 3.444 |
| | 8 - 9 | 3.089 | 3.370 | 3.066 | 3.289 | 3.111 | 3.444 |
| | 3 - 12 | 3.016 | 3.242 | 3.007 | 3.200 | 2.996 | 3.180 |
| | 6 - 9 | 3.017 | 3.242 | 3.004 | 3.198 | 2.995 | 3.181 |

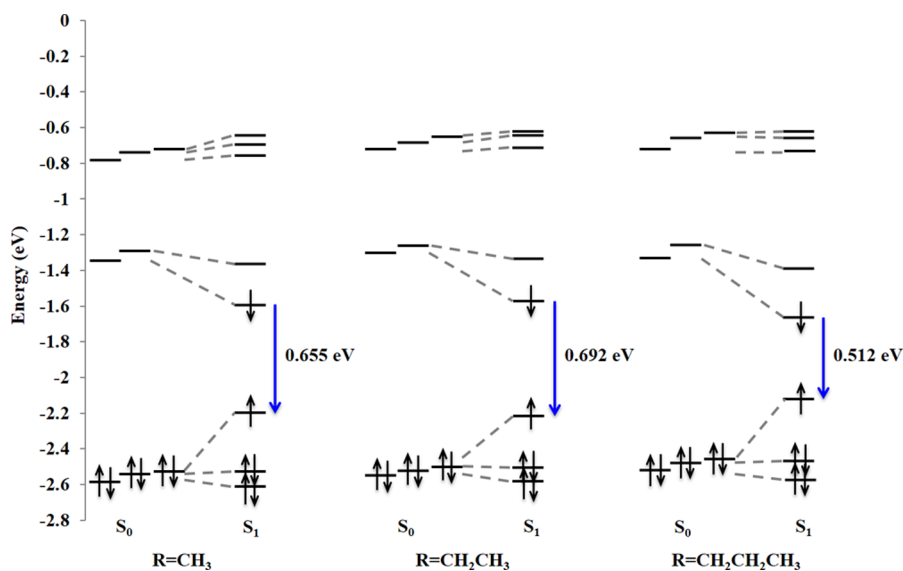


Figure 5. Comparison of energy levels of the frontier orbitals in S_0 and S_1 states of $\text{Au}_{25}(\text{SR})_{18}^-$ clusters. The S_1 state is shown in a cartoon representation with a single electron in one of the D orbitals. Dashed lines are drawn to show the splitting of triply degenerate HOMO/HOMO-1/HOMO-2, doubly degenerate LUMO/LUMO+1, and triply degenerate LUMO+2/LUMO+3/LUMO+4 orbitals of the ground state upon photoexcitation.

As suggested by the low emission energy and the large Stokes shift, the $\text{Au}_{25}(\text{SCH}_2\text{CH}_2\text{CH}_3)_{18}^-$ cluster has undergone the most geometric and electronic structure changes upon excitation. On the contrary, the highest emission energy and the lowest Stokes shift are observed for the $\text{Au}_{25}(\text{SCH}_2\text{CH}_3)_{18}^-$ cluster. This can be attributed to the relatively smaller bond length changes and frontier orbital energy level changes of this cluster. Thus, longer ligands appear to control luminescence via their effects on the geometry and electronic structure of the gold core.

Relatively small changes in emission energy are observed between the alkyl ligands examined in this work. A larger change is noted for the alkyl ligands relative to the small SH model ligand. Studies including larger ligands are of interest to

elucidate the differences previously observed between nanoparticles with phenylethylthiol ligands and those with the glutathione ligand. At present, open questions exist about the role of ligands on the emission energies and intensities, as well as the potential impact of solvent (aqueous or organic) on these items. Nonetheless, this study demonstrates the intriguing geometrical and electronic changes that occur in the $\text{Au}_{25}(\text{SR})_{18}^-$ nanoparticle upon photoexcitation.

CONCLUSIONS

DFT and TD-DFT calculations were performed to investigate the origin of photoluminescence of $\text{Au}_{25}(\text{SR})_{18}^-$ ($R = \text{H}, \text{CH}_3, \text{CH}_2\text{CH}_3, \text{CH}_2\text{CH}_2\text{CH}_3$) nanoclusters in the gas phase. The Au-Au bonds in the Au_{13} icosahedral shell expand slightly on

average in the first excited state as compared to the ground-state geometry. However, the bonds do not expand uniformly, with some bond lengths increasing by up to 0.33 Å. As a result, the shell becomes less symmetrical causing an increased splitting among HOMO/HOMO-1/HOMO-2 orbitals and the LUMO/LUMO+1 orbitals, which were approximately triply and doubly degenerate, respectively, in the ground state. In consequence, the geometrical changes in the structure lead to significant changes in the electronic structure. Stokes shifts of 0.49, 0.58, 0.56, and 0.68 eV are observed for Au₂₅(SR)₁₈⁻ (R = H, CH₃, CH₂CH₃, CH₂CH₂CH₃) nanoclusters, respectively. The nuclear relaxation after photoexcitation gives rise to vibrational beating observed in the 75–80 cm⁻¹ range.

Higher excited-state calculations suggest that several states could be responsible for the observed emission of Au₂₅(SH)₁₈⁻. The lowest calculated state that lies around 0.8 eV is populated from photoexcitation into S₁ or S₂, or transitions from higher states into these states. Two other states around 1.15 and 1.25 eV are populated from photoexcitation into S₃ or S₄ and S₅ or S₆ or transitions from higher energy states into these states. The calculated states agree well with the experimentally observed emission in the 1.15–1.55 eV range, when the typical underestimation of GGA calculations is considered.

Overall, several excited states are involved in the photoemission from Au₂₅(SR)₁₈⁻ nanoclusters. All of these excited states arise from excitations out of superatom P orbitals into the lowest two superatom D orbitals, which are core-based transitions. No charge-transfer or semi-ring states are observed in this work, which suggests that ligands primarily affect luminescence via their interactions with the gold nanoparticle core.

■ ASSOCIATED CONTENT

Supporting Information

The Supporting Information is available free of charge on the ACS Publications website at DOI: 10.1021/jacs.6b05293.

A summary of experimental photoluminescence data of Au₂₅, ground-state Kohn–Sham orbitals and significant geometrical changes upon photoexcitation of the Au₂₅(SH)₁₈⁻ nanocluster, ligand effects on ground- and excited-states electronic structures, and excitation energies of Au₂₅(SR)₁₈⁻ (R = CH₃, CH₂CH₃, CH₂CH₂CH₃) nanoclusters (PDF)

■ AUTHOR INFORMATION

Corresponding Author

*cmaikens@ksu.edu

Notes

The authors declare no competing financial interest.

■ ACKNOWLEDGMENTS

This material is based on work supported by the Department of Energy under Grant DE-SC0012273. C.M.A. is grateful to the Camille and Henry Dreyfus Foundation for a Camille Dreyfus Teacher-Scholar Award (2011–2016). The computing for this project was performed on the Beocat Research Cluster at Kansas State University, which is funded in part by NSF grants CNS-1006860, EPS-1006860, and EPS-0919443.

■ REFERENCES

- (1) Zhang, Y.; Chu, W.; Foroushani, A.; Wang, H.; Li, D.; Liu, J.; Barrow, C.; Wang, X.; Yang, W. *Materials* **2014**, *7*, 5169.
- (2) Yang, X.; Yang, M.; Pang, B.; Vara, M.; Xia, Y. *Chem. Rev.* **2015**, *115*, 10410.
- (3) Herzog, A. A.; Kiely, C. J.; Carley, A. F.; Landon, P.; Hutchings, G. J. *Science* **2008**, *321*, 1331.
- (4) Liu, Y.; Tsunoyama, H.; Akita, T.; Xie, S.; Tsukuda, T. *ACS Catal.* **2011**, *1*, 2.
- (5) Yamazoe, S.; Koyasu, K.; Tsukuda, T. *Acc. Chem. Res.* **2014**, *47*, 816.
- (6) Ide, Y.; Matsuoka, M.; Ogawa, M. *J. Am. Chem. Soc.* **2010**, *132*, 16762.
- (7) Sarina, S.; Waclawik, E. R.; Zhu, H. *Green Chem.* **2013**, *15*, 1814.
- (8) Primo, A.; Corma, A.; Garcia, H. *Phys. Chem. Chem. Phys.* **2011**, *13*, 886.
- (9) Alvaro, M.; Cojocaru, B.; Ismail, A. A.; Petrea, N.; Ferrer, B.; Harraz, F. A.; Parvulescu, V. I.; Garcia, H. *Appl. Catal., B* **2010**, *99*, 191.
- (10) Zheng, J.; Zhou, C.; Yu, M.; Liu, J. *Nanoscale* **2012**, *4*, 4073.
- (11) Yu, Y.; Luo, Z.; Chevrier, D. M.; Leong, D. T.; Zhang, P.; Jiang, D.-e.; Xie, J. *J. Am. Chem. Soc.* **2014**, *136*, 1246.
- (12) Xie, J.; Zheng, Y.; Ying, J. Y. *J. Am. Chem. Soc.* **2009**, *131*, 888.
- (13) Mooradian, A. *Phys. Rev. Lett.* **1969**, *22*, 185.
- (14) Wilcoxon, J. P.; Martin, J. E.; Parsapour, F.; Wiedenman, B.; Kelley, D. F. *J. Chem. Phys.* **1998**, *108*, 9137.
- (15) Mohamed, M. B.; Volkov, V.; Link, S.; El-Sayed, M. A. *Chem. Phys. Lett.* **2000**, *317*, 517.
- (16) Bigioni, T. P.; Whetten, R. L.; Dag, Ö. *J. Phys. Chem. B* **2000**, *104*, 6983.
- (17) Huang, T.; Murray, R. W. *J. Phys. Chem. B* **2001**, *105*, 12498.
- (18) Wang, G.; Huang, T.; Murray, R. W.; Menard, L.; Nuzzo, R. G. *J. Am. Chem. Soc.* **2005**, *127*, 812.
- (19) Negishi, Y.; Nobusada, K.; Tsukuda, T. *J. Am. Chem. Soc.* **2005**, *127*, 5261.
- (20) Negishi, Y.; Takasugi, Y.; Sato, S.; Yao, H.; Kimura, K.; Tsukuda, T. *J. Am. Chem. Soc.* **2004**, *126*, 6518.
- (21) Zhu, M.; Aikens, C. M.; Hollander, F. J.; Schatz, G. C.; Jin, R. *J. Am. Chem. Soc.* **2008**, *130*, 5883.
- (22) Heaven, M. W.; Dass, A.; White, P. S.; Holt, K. M.; Murray, R. W. *J. Am. Chem. Soc.* **2008**, *130*, 3754.
- (23) Akola, J.; Walter, M.; Whetten, R. L.; Häkkinen, H.; Grönbeck, H. *J. Am. Chem. Soc.* **2008**, *130*, 3756.
- (24) Link, S.; Beeby, A.; FitzGerald, S.; El-Sayed, M. A.; Schaaff, T. G.; Whetten, R. L. *J. Phys. Chem. B* **2002**, *106*, 3410.
- (25) Link, S.; El-Sayed, M. A.; Gregory Schaaff, T.; Whetten, R. L. *Chem. Phys. Lett.* **2002**, *356*, 240.
- (26) Schaaff, T. G.; Whetten, R. L. *J. Phys. Chem. B* **2000**, *104*, 2630.
- (27) Schaaff, T. G.; Knight, G.; Shafiqullin, M. N.; Borkman, R. F.; Whetten, R. L. *J. Phys. Chem. B* **1998**, *102*, 10643.
- (28) Lee, D.; Donkers, R. L.; Wang, G.; Harper, A. S.; Murray, R. W. *J. Am. Chem. Soc.* **2004**, *126*, 6193.
- (29) Shibu, E. S.; Pradeep, T. *Int. J. Nanosci.* **2009**, *08*, 223.
- (30) Shibu, E. S.; Muhammed, M. A. H.; Tsukuda, T.; Pradeep, T. *J. Phys. Chem. C* **2008**, *112*, 12168.
- (31) Green, T. D.; Yi, C.; Zeng, C.; Jin, R.; McGill, S.; Knappenberger, K. L. *J. Phys. Chem. A* **2014**, *118*, 10611.
- (32) Miller, S. A.; Womick, J. M.; Parker, J. F.; Murray, R. W.; Moran, A. M. *J. Phys. Chem. C* **2009**, *113*, 9440.
- (33) Qian, H.; Y. Sfeir, M.; Jin, R. *J. Phys. Chem. C* **2010**, *114*, 19935.
- (34) Wang, G.; Guo, R.; Kalyuzhny, G.; Choi, J.-P.; Murray, R. W. *J. Phys. Chem. B* **2006**, *110*, 20282.
- (35) Wu, Z.; Jin, R. *Nano Lett.* **2010**, *10*, 2568.
- (36) Wang, S.; Zhu, X.; Cao, T.; Zhu, M. *Nanoscale* **2014**, *6*, 5777.
- (37) Devadas, M. S.; Kim, J.; Sinn, E.; Lee, D.; Goodson, T.; Ramakrishna, G. *J. Phys. Chem. C* **2010**, *114*, 22417.
- (38) Ramakrishna, G.; Varnavski, O.; Kim, J.; Lee, D.; Goodson, T. *J. Am. Chem. Soc.* **2008**, *130*, 5032.

- (39) Yau, S. H.; Varnavski, O.; Gilbertson, J. D.; Chandler, B.; Ramakrishna, G.; Goodson, T. *J. Phys. Chem. C* **2010**, *114*, 15979.
- (40) te Velde, G.; Bickelhaupt, F. M.; Baerends, E. J.; Fonseca Guerra, C.; van Gisbergen, S. J. A.; Snijders, J. G.; Ziegler, T. *J. Comput. Chem.* **2001**, *22*, 931.
- (41) Becke, A. D. *Phys. Rev. A: At., Mol., Opt. Phys.* **1988**, *38*, 3098.
- (42) Perdew, J. P. *Phys. Rev. B: Condens. Matter Mater. Phys.* **1986**, *33*, 8822.
- (43) Aikens, C. M. *J. Phys. Chem. A* **2009**, *113*, 10811.
- (44) Guidez, E. B.; Aikens, C. M. *J. Phys. Chem. A* **2015**, *119*, 3337.
- (45) Chen, S.; Wang, S.; Zhong, J.; Song, Y.; Zhang, J.; Sheng, H.; Pei, Y.; Zhu, M. *Angew. Chem., Int. Ed.* **2015**, *54*, 3145.
- (46) Bae, G.-T.; Aikens, C. M. *J. Phys. Chem. C* **2015**, *119*, 23127.
- (47) Hulkko, E.; Lopez-Acevedo, O.; Koivisto, J.; Levi-Kalisman, Y.; Kornberg, R. D.; Pettersson, M.; Häkkinen, H. *J. Am. Chem. Soc.* **2011**, *133*, 3752.
- (48) Liao, M.-S.; Bonifassi, P.; Leszczynski, J.; Ray, P. C.; Huang, M.-J.; Watts, J. D. *J. Phys. Chem. A* **2010**, *114*, 12701.
- (49) Aikens, C. M.; Li, S.; Schatz, G. C. *J. Phys. Chem. C* **2008**, *112*, 11272.
- (50) Costa, P. J.; Calhorda, M. J. *Inorg. Chim. Acta* **2006**, *359*, 3617.
- (51) Bode, B. M.; Gordon, M. S. *J. Mol. Graphics Modell.* **1998**, *16*, 133.
- (52) Aikens, C. M. *J. Phys. Chem. C* **2008**, *112*, 19797.
- (53) Aikens, C. M. *J. Phys. Chem. Lett.* **2011**, *2*, 99.
- (54) Walter, M.; Akola, J.; Lopez-Acevedo, O.; Jadzinsky, P. D.; Calero, G.; Ackerson, C. J.; Whetten, R. L.; Grönbeck, H.; Häkkinen, H. *Proc. Natl. Acad. Sci. U. S. A.* **2008**, *105*, 9157.
- (55) Marques, M. A. L.; Castro, A.; Rubio, A. *J. Chem. Phys.* **2001**, *115*, 3006.
- (56) Tofanelli, M. A.; Salorinne, K.; Ni, T. W.; Malola, S.; Newell, B.; Phillips, B.; Häkkinen, H.; Ackerson, C. J. *Chem. Sci.* **2016**, *7*, 1882.